PAPER

Check for updates

Facile supramolecular strategy to construct solid fluorophore@metal–organic framework composites†

Lavinia A. Trifoi, Gregory K. Hodgson, [ID] Nicholas P. Dogantzis, [ID] Sumaiya A. Soha, Roya M. Dayam, Costin N. Antonescu, Roberto J. Botelho, R. Stephen Wylie and Stefania Impellizzeri [ID] *

The design and synthesis of a microporous construct based on the entrapment of an emissive fluorescein derivative in a zinc 2-methylimidazolate (ZIF-8) metal–organic framework (MOF) is detailed. Synthesis of the MOF in the presence of a fluorophore enables the capture and dispersal of dye molecules within the framework. Within the resulting supramolecular assemblies, the fluorophore components show excellent photophysical properties such as high emission and increased fluorescence lifetime, despite the tendency of the dye to undergo aggregation-caused quenching in the solid-state, as well as a 4-fold enhancement of the fluorophore's photostability. The demonstration that supramolecular events can be invoked to construct solid fluorescent systems from separate components is realized. The encapsulation of the fluorescein in an enclosed subunit of the ZIF-8 framework was modelled using the density-functional tight-binding method. Furthermore, the fluorophore@MOF composite can be internalized by mammalian macrophage cells and transported to lysosomes without disrupting cell viability. In principle, this simple protocol can evolve into a general strategy for intracellular delivery of functional molecular components for targeted bioimaging or theranostic applications.

Laboratory for Nanomaterials and Molecular Plasmonics, Department of Chemistry and Biology, Toronto Metropolitan University, Toronto, Ontario, M5B 2K3, Canada. E-mail: simpellizzeri@ryerson.ca

† Electronic supplementary information (ESI) available: ^{1}H and ^{13}C NMR of **FMe520**. Calculation of the molar extinction coefficient of **FMe520**. Synthesis of **FMe520**@ZIF-8 and calculation of the encapsulation efficiency. Calculation of the adsorption efficiency of **FMe520** on pre-formed ZIF-8. Emission spectra and photographs of **FMe520**@ZIF-8 in CH₃OH stirred for 7 days. Scanning electron microscopy (SEM) and size distribution of ZIF-8 particles. Scanning electron microscopy (SEM) and size distribution of **FMe520**@ZIF-8 particles. FTIR-ATR spectra of ZIF-8 and **FMe520**@ZIF-8. Electrospray ionization mass spectrometry of **FMe520**, ZIF-8 and **FMe520**@ZIF-8. Absorption of **FMe520**@ZIF-8 before and after addition of HCl. Absorption of **FMe520** before and after addition of HCl. Photographs of **FMe520**@ZIF-8, **FMe520** and ZIF-8 under ultraviolet light. Average fluorescence lifetimes of **FMe520** and **FMe520**@ZIF-8. Raw FLIM data for **FMe520**. Raw FLIM data for **FMe520**@ZIF-8. Emission spectra of **FMe520**@ZIF-8 and **FMe520** before and after irradiation at 455 nm. Zn–N bond distances in ZIF-8. Four conformers of **FMe520**. Boltzmann-averaged fractional abundances of **FeMe520** conformers. Energy differences (SCC-DFTB) between optimized **FMeF520** conformer-cage complexes and the sums of the separated components. Four examples of stabilized ZIF-8 cage complexes of **FMe520**. See DOI: https://doi.org/10.1039/d2ma00548d

Introduction

Metal–organic frameworks (MOFs) are attractive candidates for the design of fluorescent nanocomposites for bioimaging applications.[1–7] MOFs are constructed *via* self-assembly of organic ligands and metal ions (or clusters).[8–11] MOFs have shown great potential for developing biosensors[2,4,12–18] and theranostic agents for tandem imaging, targeting, and cargo delivery[19–23] due to their tunable composition and structural flexibility, good biocompatibility, biodegradability, and low cytotoxicity.[1,24–28] The identity and distribution of surface functionality can be controlled through simple post-synthetic modifications.[29–32] Moreover, the size of MOFs can be selectively scaled down to the nanoscale, which can facilitate intracellular accumulation *via* endocytosis.[25,27,33,34]

Fluorescence in MOFs can be generated from its components – the metal and ligands – and tuned through the interplay between them.[35–47] Nonetheless, the high and permanent porosity of MOFs also enables the encapsulation of emissive guest molecules.[48–54] This approach can help overcome common issues with using synthetic fluorophores for biological applications. For example, most fluorophores are rather hydrophobic and can only be dissolved in apolar organic solvents. Furthermore, it is unclear whether the key photochemical and photophysical properties of the probes can survive the transition from organic to aqueous environments necessary for their application in biological research. Thus, it is imperative to identify viable strategies to impose biocompatibility on

fluorescent probes, without complicating their synthesis, and to effectively operate these functional compounds under physiological conditions. In this context, the selective encapsulation of fluorophores in porous particles like MOFs can lead to the formation of an emissive nanocomposite material in which the encapsulated probe is bestowed with desirable photophysical properties. These can include such aspects as photostability, high quantum yields, increased excited state lifetimes and better organization of the dye molecules. MOF encapsulation may also simultaneously provide a convenient solution to the low biocompatibility or scarce solubility of the dye under biological conditions and/or aggregation- or concentration-caused quenching phenomena.[55]

Based on these considerations, we report on a model fluorescent compound **FMe520** (Fig. 1) and investigate the possibility of invoking supramolecular events to improve on the photophysical properties of this hydrophobic species. This is achieved by encapsulating **FMe520** into the popular zinc 2-methylimidazolate $Zn(MeIm)_2$ (ZIF-8)[56–61] as the host MOF.[62,63] ZIFs are a common choice for the design of molecular (*e.g.*, dyes or drugs) delivery systems, due to their biocompatibility and enhanced stability in aqueous or physiological conditions that facilitates cellular uptake while avoiding premature content release.[64] Their relatively large available pores, which can accommodate significant amounts of the guest compound, is an additional structural advantage.[11] In addition, the optical transparency of ZIF-8 in the visible and near-infrared regions oʻf the electromagnetic spectrum (*vide infra*) is an asset for imaging purposes. The model fluorophore **FMe520** was chosen as a suitable representative of a family of modified organic dyes

that can be easily prepared from commercial fluorescein (Fig. 1). Indeed, fluorescent probes based on the fluorescein platform possess favourable properties for application in fluorescence microscopy, such as excitation and emission wavelengths in the visible region and high fluorescence quantum yield.[65] Free fluorescein transport across cell membranes occurs in part *via* saturable protein-mediated transport.[66,67] In contrast, the accumulation of this dye encapsulated into a MOF particle within cells is unlikely to occur by the same mechanism as the free dye, and rather undergoes endocytosis. In turn, this allows delivery and targeting of the florescent reporter to endo-lysosomal membrane compartments. We chose to modify fluorescein by conversion of the phenolic and carboxylic acid groups to the corresponding methyl ether and methyl ester, respectively. This was done to avoid difficulties to model non-covalent interaction (*e.g.*, H-bonding), truncate the effects of external pH variations, and avoid complications related to the different prototropic forms of fluorescein. Herein, we report the synthesis and characterization of these hybrid **FMe520**@ZIF-8 composites, computational modelling of encapsulated **FMe520**, and the investigation of their cytotoxicity and ability to cross cell membranes. This works serves as a proof of principle for the future applications of such materials in bioprobe design.

Results and discussion

Design and synthesis of FMe520 and FMe520@ZIF-8

The methylated fluorescein **FMe520** (Fig. 1) was synthesized in one step starting from commercially available fluorescein.[68] Alkylation with methyl iodide gave methyl 2-(6-methoxy-3-oxo-3*H*-xanthen-9-yl)benzoate (**FMe520**) in a 23% yield after purification (see Experimental). The product was characterized by ^{1}H and ^{13}C NMR (Fig. S1, ESI†). The absorption spectrum of a solution of **FMe520** in CH_3OH shows a band at $\lambda_{Abs} = 455$ nm (Fig. 1A). The molar extinction coefficient of **FMe520** is $\sim 32\,000$ M^{-1} cm^{-1} (CH_3OH solution at λ_{max}: Fig. S2, ESI†). Moreover, compound **FMe520** is fluorescent at $\lambda_{Em} = 520$ nm (Fig. 1B) under similar conditions. The spectroscopic signature of **FMe520** is thus identical to that of common fluorescein.[65]

A comparison between the pore and channel size of the zinc 2-methylimidazolate $Zn(MeIm)_2$ (ZIF-8) framework to the molecular dimensions of **FMe520** (A in Fig. 2) reveals that our chromophore cannot be readily introduced into ZIF-8 by simple soaking[53,69–71] of the pre-synthesized MOF in a solution of the dye.[72,73] Although a ZIF-8 pore can enclose a ~ 12 Å diameter sphere (B in Fig. 2), and should therefore be large enough to host a molecule of **FMe520**, the larger pores are connected by channels of only 3.4 Å in diameter. Thus, in order to encapsulate the fluorescent component, we performed an *in situ* synthesis of the metal–organic framework in the direct presence of guest **FMe520**.[74,75] Dissolution of **FMe520** and 2-methyl imidazole in CH_3OH, followed by the addition of $Zn(NO_3)_2 \cdot 6H_2O$ (C in Fig. 2) and resting at room temperature for 48 h in the dark encourages permanent entrapment of the chromophore into ZIF-8. The resulting material was washed and centrifuged
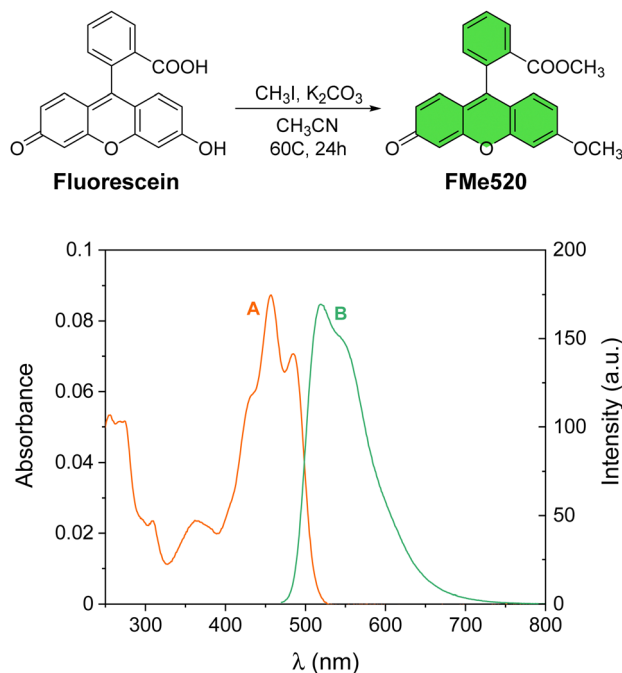

Fig. 1 Preparation of the model fluorophore **FMe520** from commercial fluorescein. Absorption (A) and emission (B) spectra of a solution of **FMe520** (3 µM, CH_3OH, 20 °C, $\lambda_{Ex} = 450$ nm).
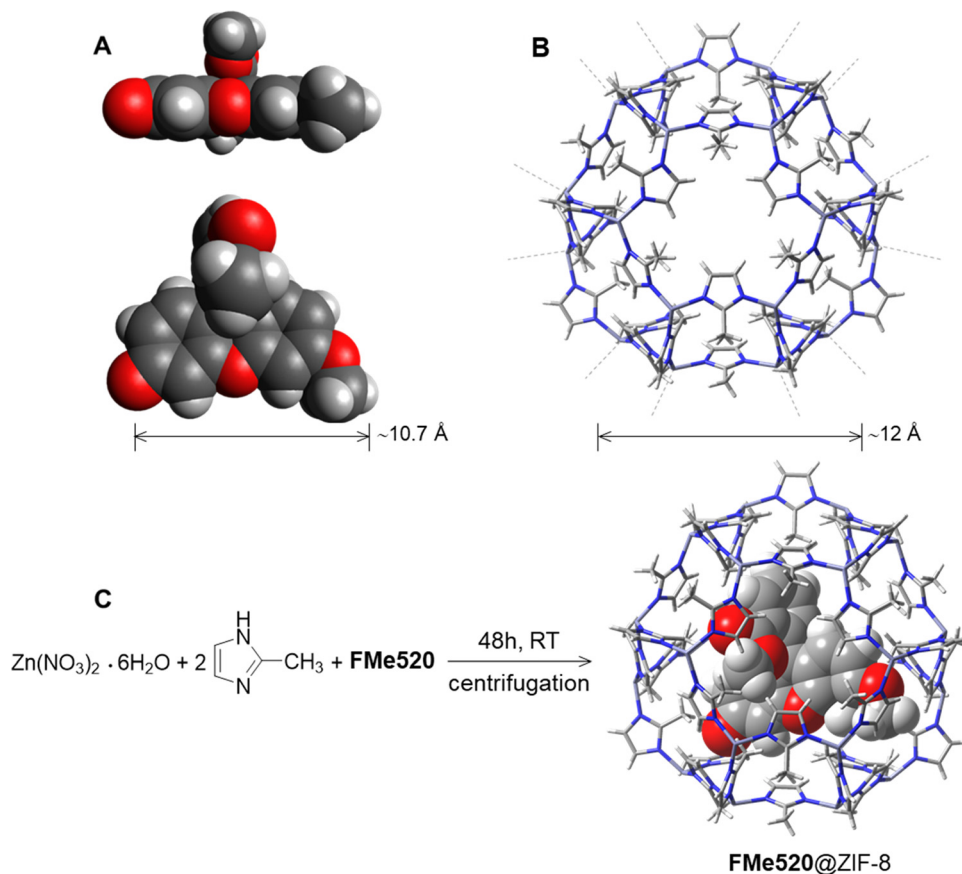
Fig. 2 Structures and relevant dimensions of (A) **FMe520** and (B) ZIF-8. The geometry of **FMe520** in A was optimized at the B3LYP/6-311 + G(d,p) level and is represented with atoms rendered as van der Waals spheres; conformer *B* is shown (*vide infra*: Molecular Modelling, and Fig. S16, ESI†). Synthesis of **FMe520**@ZIF-8 (C).

until the absorbance of the supernatant showed no residual signal from the fluorophores. In parallel, the empty ZIF-8 was prepared under identical conditions in the absence of dye. We estimated a dye encapsulation efficiency of ~43% over a 48 h crystallization period (see ESI† and related discussion) using the known molar extinction coefficient of **FMe520** and by measuring the absorbance of the combined supernatant solutions obtained after several CH_3OH washing cycles. For this work, we did not seek to repeat the process with variable guest concentrations: however, crystallization of the metal–organic framework in the presence of the guest fluorophore for 24 h reduced the encapsulation efficiency to ~22%. The retention of the absorption and emissive properties of the solid material after purification (*vide infra*) indicated that the dyes are permanently trapped into the ZIF-8 pores, rather than adsorbed on the external surface. Nonetheless, to quantify the possibility of surface adherence of the fluorophore to the outer framework, we separately attempted the adsorption of **FMe520** to pre-formed ZIF-8. The latter was accomplished by mixing **FMe520** to a dispersion of empty ZIF-8 in CH_3OH and stirring for 48 h. To avoid bias, we kept the dye/MOF mass ratio roughly the same as when ZIF-8 is crystallized *in situ* in the presence of the fluorescent guest. The adsorption time was also kept at 48 h. Following identical washing and centrifugation, and using

spectrometric methods, we estimated the maximum efficiency of **FMe520**'s adsorption onto the external surface of the metal–organic framework to be about 7% (see ESI† and related discussion). Leaching of the dye content from encapsulated **FMe520**@ZIF-8 was monitored over a week, by gently stirring a suspension of the composite in CH_3OH and measuring the emission signature of the solvent. Emission spectra were recorded using identical excitation conditions and emission slits to check for free **FMe520** which, unlike **FMe520**@ZIF-8, is very soluble in CH_3OH. Results show that the small dimension of the pore channels prevents significant amounts of guest dye from escaping the MOF cage (Fig. S5, ESI,† where it is noted that the low number of counts indicates that no dye is dissolved).

Structural characterization and photophysical properties of FMe520@ZIF-8

The size and morphology of the prepared materials were observed by scanning electron microscopy (SEM). As shown in Fig. 3, ZIF-8 particles display a typical rhombic dodeca-hedron morphology with an average particle size of 270 nm (A in Fig. 3 and Fig. S6, ESI†). Intriguingly, while the morphology of **FMe520**@ZIF-8 crystals appears mainly unchanged after dye loading, their size is roughly a third of the unloaded
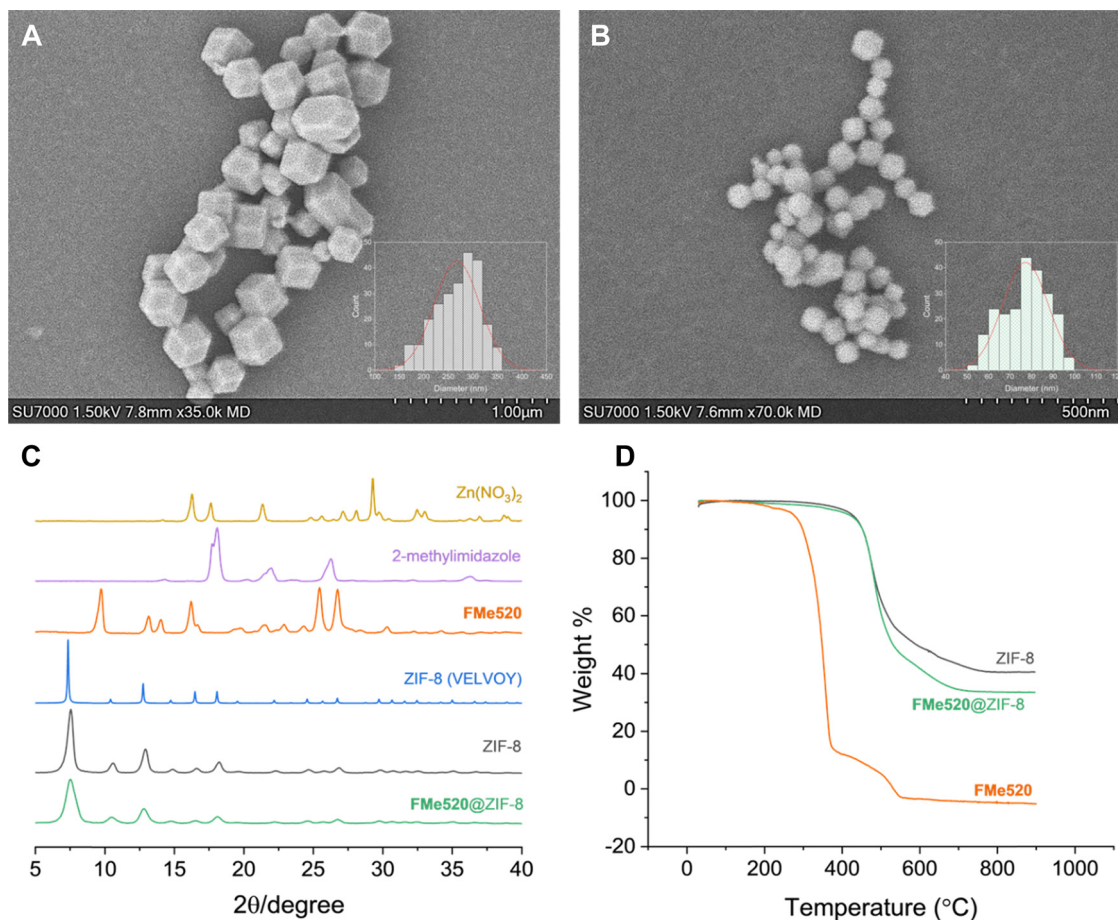
Fig. 3 Scanning Electron Microscopy (SEM) of (A) ZIF–8 and (B) **FMe520**@ZIF–8 particles crystallized over 48 h. For full-size distribution histograms, see Fig. S6 and S7 (ESI†). (C) Selected PXRD patterns for $Zn(NO_3)_2$, 2-methylimidazole, solid **FMe520**, simulated for ZIF-8 (CSD code VELVOY), ZIF-8, and **FMe520**@ZIF-8. (D) TGA thermograms of ZIF-8, **FMe520**@ZIF-8, and solid **FMe520** conducted in a dynamic atmosphere of air.

particles (B in Fig. 3 and Fig. S7, ESI†). The presence of the dye may enhance the MOF's nucleation rate, resulting in decreased crystal size distributions.[76] This result poses the excellent question of deliberately envisioning the use of small fluorescent probes as 'non-innocent' guest molecules as a component of framework design for the strategic downsizing of typically large MOF crystals into their nanosized versions. More work is currently underway to determine more quantitatively how bottom-up dye encapsulation can contribute to the rational design of nanosized MOFs, which would be an asset for bioimaging applications. The main peaks of the powder X-ray diffraction (PXRD) pattern of **FMe520**@ZIF-8 are an excellent match to the pattern of ZIF-8, while no peaks attributable to 'free' **FMe520** were observed (C in Fig. 3). These results additionally demonstrate that **FMe520** was successfully introduced into ZIF-8 and retained within the framework and that the unit cell geometries are unchanged for the regular (without dye) and downsized (with dye) MOF crystals. Thermal gravimetric analysis (TGA) performed on **FMe520**@ZIF-8 reveals the remarkable thermal stability of this material (D in Fig. 3). Indeed, while the organic fluorophore **FMe520** starts to decompose at $\sim$250 °C, the same species encapsulated in ZIF-8 is stable up to

450 °C, similar to the empty crystalline framework. Vibrational modes in ZIF-8 and **FMe520**@ZIF-8 FTIR spectra remain practically identical, with the peak at 1725 cm^{-1} attributed to the C$=$O vibrational model of **FMe520** disappearing after confinement (Fig. S8, ESI†). Electrospray ionization mass spectrometry conducted on samples of **FMe520**, ZIF-8, and **FMe520**@ZIF-8 also confirms the structural integrity of the nanocomposite (Fig. S9, ESI†). We then attempted to calculate the ratio of **FMe520**/2-methylimidazole using NMR spectroscopy. In brief, 3 drops of aqueous HCl were added to **FMe520**@ZIF-8 with deuterated dimethyl sulfoxide (DMSO-d_6) and analyzed by ^{1}H NMR. Despite an immediate change in coloration from pale yellow to bright yellow, suggesting the release of the highly soluble fluorophore into the solvent, we could not detect signals attributable to **FMe520** in the NMR spectrum of the digested material. The resulting ^{1}H NMR spectrum shows instead the resonances typical of the dissolved MOF components. Nonetheless, the discharge in the solution of the encapsulated fluorophore **FMe520** from the dissolved MOF can be easily detected by absorption spectroscopy. In fact, while **FMe520**@ZIF-8 is not very soluble in CH_3OH (as illustrated by the photographs in Fig. S5, ESI†), incremental addition of HCl
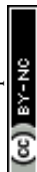
induces the breakdown of the zeolitic framework, concomitantly releasing the guest molecules in solution. The process is accompanied by an increase in the typical absorption of **FMe520** in an acidic environment (Fig. S10, ESI†), the latter causing a partial loss of the vibrational structure of the band. This trend is also observed in control experiments performed by adding acid to a CH$_3$OH solution of **FMe520** in the absence of the MOF (Fig. S11, ESI†). Note that the acid digestion experiment was conducted on a sample of **FMe520**@ZIF-8 with 22% dye encapsulation efficiency (from 24 h crystallization). From the molar extinction coefficient

value of **FMe520-H$^+$** (*i.e.*, **FMe520** in acidic environment) extracted from Fig. S11 (ESI†), we recalculated that the concentration of **FMe520** released from the digested MOF is in excellent agreement with our previous estimate of the dye encapsulation efficiency.

The molecular components entrapped within the metal–organic framework retain their photophysical properties. **FMe520**@ ZIF-8 appears as a yellow-coloured powder (A in Fig. 4), and its diffuse reflectance spectrum (green trace in Fig. 4C) displays the characteristic absorption signature of **FMe520** in the visible region. In contrast, the empty ZIF-8 framework is a white powder
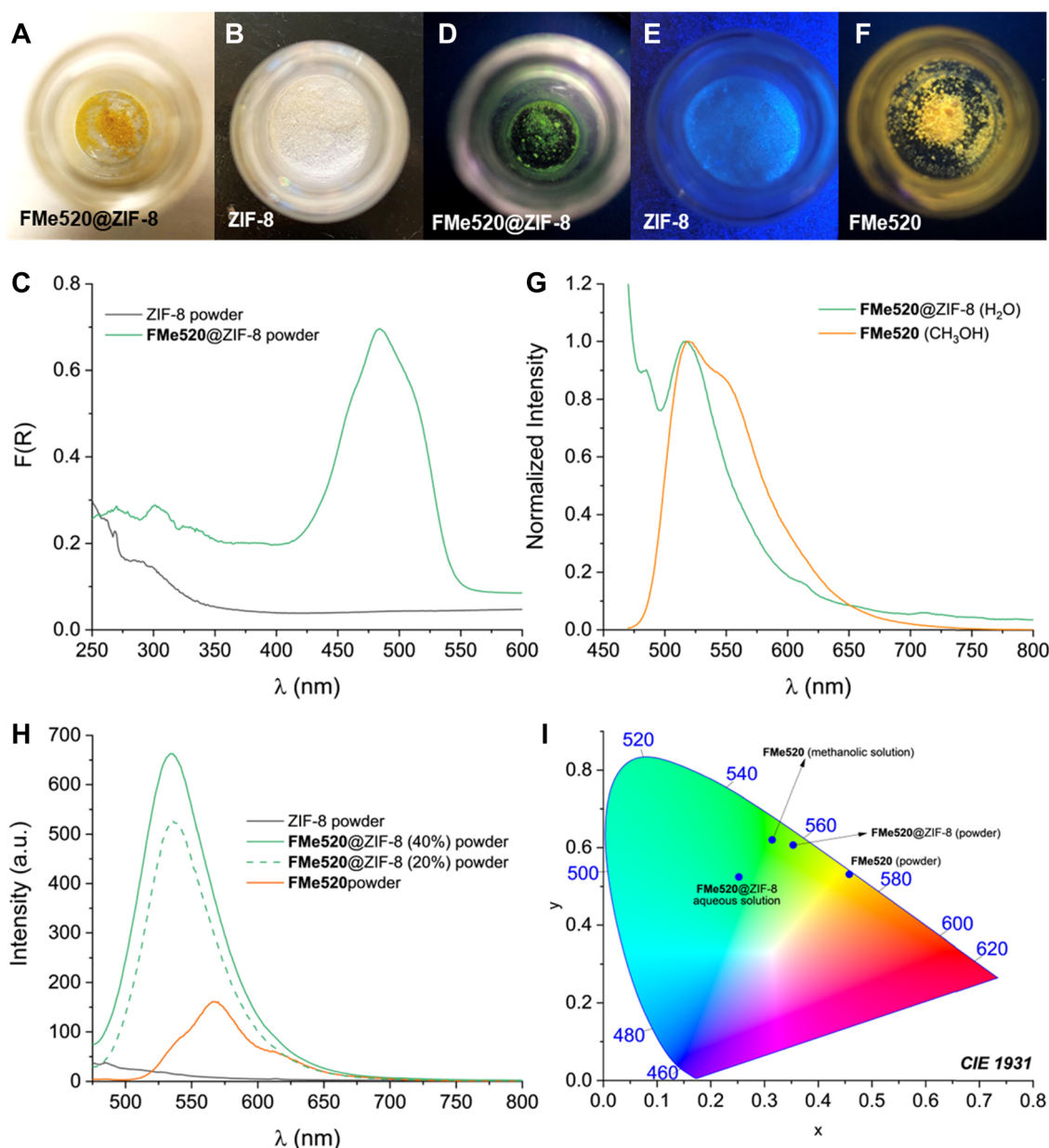

Fig. 4 Samples of (A) **FMe520**@ZIF-8 and (B) ZIF-8 viewed under ambient light. (C) Diffuse reflectance of **FMe520**@ZIF-8 (green trace) and ZIF-8 (black trace) powders. Diffuse reflectance of solid **FMe520** (not shown) has a max. at 432 nm. Samples of (D) **FMe520**@ZIF-8, (E) ZIF-8, and (F) **FMe520** viewed under ultraviolet light (see also Fig. S12, ESI†). (G) Normalized emission spectra (20 °C, λ_{Ex} = 450 nm) of a filtered aqueous solution of **FMe520**@ZIF-8 (green trace) and methanolic solution of **FMe520** (orange trace). (H) Emission spectra recorded at the solid-state of ZIF-8 (black trace), **FMe520**@ZIF-8 (green traces), and solid **FMe520** (orange trace). (I) Emission wavelengths of **FMe520** in CH$_3$OH solution, **FMe520**@ZIF-8 in H$_2$O, **FMe520**@ZIF-8 powder, and **FMe520** powder charted as colour coordinates in a CIE 1931 chromaticity diagram.

(B in Fig. 4) with no distinctive absorption or emission in the visible region of the spectrum (black trace in Fig. 4C and H, respectively). On the other hand, **FMe520@ZIF-8** is visibly fluorescent under ultraviolet light (D in Fig. 4): its emission spectra exhibit the typical fluorescence of **FMe520** at λ_{Em} = 520 nm in aqueous solution, which coincides with that of **FMe520** in CH$_3$OH (Fig. 4G). At the solid state, the emission of **FMe520@ZIF-8** is centred at 535 nm, while the emission of solid **FMe520** has a maximum at 570 nm (Fig. 4H). All the corresponding luminescent colour coordinates were calculated and plotted in a CIE 1931 chromaticity diagram (I in Fig. 4). The emission behaviour of **FMe520** alone is consistent with increased stracking behaviour and the formation of aggregates and dense interchromophore interactions at the solid-state. Indeed, molecules having 'rotatable groups' (such as **FMe520**, which carries a phenyl ring attached to the xanthene core) tend to attain planarity in the solid state. In turn, this increases their conjugation and causes a bathocromic (red) shift of their emission. This is in contrast with the behaviour of **FeM520** in solution, where the dye adopts a configuration in which the phenyl ring has nearly perpendicular orientation with respect to the xanthene core (*vide infra*, Molecular Modelling). Interestingly, the emission of **FMe520@ZIF-8** at 535 nm implies that the zeolitic cage inhibits the occurrence of dye–dye interactions, and even prevents the encapsulated fluorophore to achieve a planar configuration. This is confirmed by SCC-DFTB calculations (once again, see Molecular Modelling). Additionally, **FMe520@ZIF-8** exhibits strong fluorescence in the solid-state (observed at both 43% and 22% dye encapsulation efficiency), while the emission intensity of non-encapsulated solid **FMe520** (F in Fig. 4 and orange trace in Fig. 4H) is substantially lower. This is expected from aggregation-caused quenching in a tightly packed environment. Thus, it appears that the organization of chromophores within the MOF can prevent aggregation and quenching.

The excellent photophysical properties of the fluorophore when encapsulated in the MOF are additionally showcased by the increased fluorescence lifetime of **FMe520@ZIF-8** compared to **FMe520**. Fluorescence lifetime imaging microscopy (FLIM) measurements report that the average lifetime of **FMe520** improves from 3.22 ns to 6.49 ns when incarcerated within ZIF-8 (A in Fig. 5; see also Fig. S13, S14, and Table S1, ESI†). Monoexponential fluorescence decays were seen for all the regions of interest (ROI) examined, indicating a single dye environment. Since the MOF does not affect the radiative decay rate of the fluorophore, the increased fluorescence lifetime of **FMe520@ZIF-8** highlights a drop in the nonradiative decay rate upon encapsulation. This is likely due to a better organization of the dye molecules in the rigid surroundings. The **FMe520@ZIF-8** solid exhibits dramatically enhanced photostability, as showed by the comparison between the rate of photobleaching for a sample of **FMe520@ZIF-8** compared to a control sample of **FMe520** (B in Fig. 5; see also Fig. S15, ESI†). Photobleaching tests were performed by recording the emission spectra of **FMe520@ZIF-8** and **FMe520** upon exposure to 455 nm LED light. After 30 min of irradiation, only 30% of the fluorescence of **FMe520** remains (orange trace in Fig. 5B), whereas 86% of
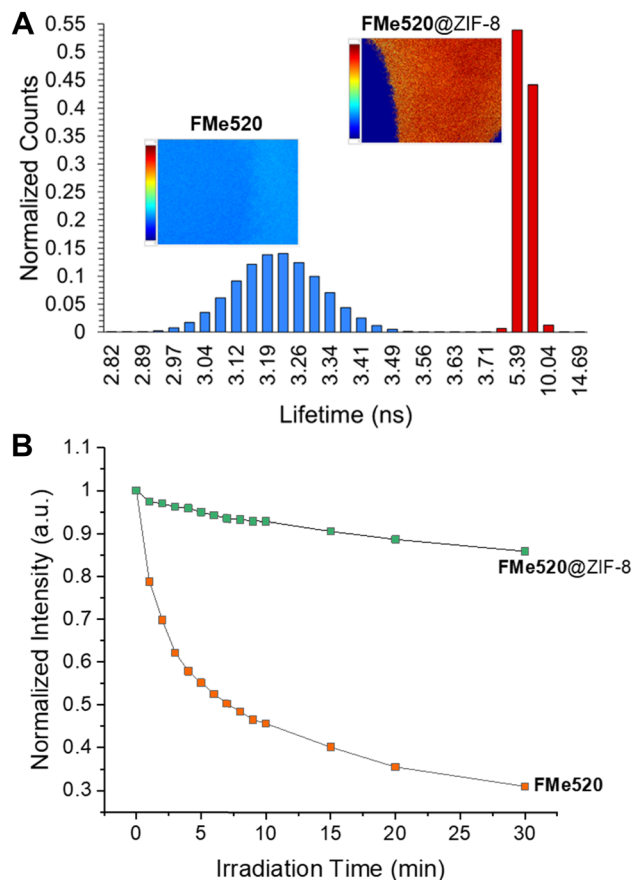

Fig. 5 (A) Fluorescence lifetime distributions for **FMe520** (blue bars) and **FMe520**@ZIF-8 (red bars), obtained by fluorescence lifetime imaging microscopy (FLIM) performed on the entire region of interest depicted by the corresponding colour coded inset image. Inset colour scales range from 2–7 ns for both images. (B) Normalized integrated emission of **FMe520**@ZIF (green squares) and **FMe520** (orange squares) upon increasing irradiation time (455 nm).

the initial intensity is observed for **FMe520@ZIF-8** under identical irradiation conditions (green trace in Fig. 5B). The curves in Fig. 5B can be fitted by an exponential decay function to estimate the photobleaching rate of **FMe520** with and without ZIF-8. Accordingly, we calculated the rates of photobleaching of the two solids to be 0.229 ± 0.030 s^{-1} and 0.0530 ± 0.0095 s^{-1} for **FMe520** and **FMe520@ZIF-8**, respectively. Overall, encapsulation of the dye into the MOF's porous structure reduces the photobleaching rate and enhances photostability by approximately four-fold due to reduced molecular mobility and aggregation, both of which would encourage accelerated dye photodegradation.[77]

Molecular Modelling of FMe520@ZIF-8

Given the difficulty of growing single crystals suitable for X-ray crystallographic analysis, molecular modelling was performed to obtain further insight into the architectural features of the fluorophore@MOF composite. Computational studies of ZIF-8 complexes can be broadly grouped into several classes: DFT calculations of interaction energies between ZIF-8 components

(Zn clusters) and small molecules,[78–81] periodic DFT calculations of the extended solid-state structures with or without guests,[81–87] and Monte Carlo simulations of small molecule adsorption and diffusion.[87–89] Our aim was to determine if **FMe520** could be encapsulated into the ZIF-8 sodalite (SOD) cage without significant destabilization and if evidence could be obtained as to the preferred orientations between the functional groups of **FMe520** and the structural elements of ZIF-8. To this end, a ZIF-8 SOD cage omitting coordinatively unsaturated imidazolate ligands was derived from crystallographic structural data; the resulting 420 atom subunit had an overall assigned charge of 12+. Geometric optimization of the empty cage using the self-consistent-charge density-functional tight-binding (SCC-DFTB) method resulted in a loss of symmetry and a slight overall shrinkage due to shorter Zn–N bonds ($\sim$0.025 Å, see Table S2, ESI†). To ensure a more spatially realistic cage structure, further optimizations used frozen cage coordinates to maintain the initial structure. Exploration of the conformational space of the **FMe520** molecule revealed four conformers (A–D, Fig. S16, ESI†) arising from two in-plane orientations of the OCH_3 substituent on the xanthene core and two orientations of the ester group. The nearly perpendicular orientation of the phenyl ring with respect to the xanthene core places either the carbonyl or methoxy group just above one face of the planar dye. Boltzmann weighting estimates that 76% of the conformers have the carbonyl group proximal to the xanthene plane (C and D) and 70% have the OCH_3 substituent oriented perpendicular to the long axis of the xanthene core (B and D); conformer D makes up 54% of the overall population (Table S3, ESI†). The steric requirements of the four conformers vary. The xanthene core ranges in length from 10.7 Å (OCH_3 perpendicular to the xanthene long axis, B and D) to 11.5 Å (OCH_3 extended along the long axis, A and C); the distances with Bondi van der Waals radii are 13.4 Å and 14.2 Å, respectively. The phenyl substituent extends the width of the xanthene core to roughly 9 Å and, due to its near-perpendicular orientation, adds around 8 Å in depth; these dimensions vary depending on the orientation of the $COOCH_3$ group on the phenyl substituent. Conformer C is the most sterically demanding, with B being the least. Given its size and shape, the **FMe520** molecule is too bulky to move through the ZIF-8 cage pores but appears to be small enough to fit inside the interior cavity. To test this computationally, we performed SCC-DFTB optimizations of **FMe520** conformers within the cage subunit in various initial positions; the cage subunit was frozen but the encapsulated **FMe520** was free to move within the cage. The SCF energies of the optimized structures were compared with the energies of the empty cage and the corresponding **FMe520** conformer by subtraction, with a positive result indicating destabilization. In a series of trials, we observed energy differences ranging from -13 to 30 kJ mol^{-1} for successfully optimized structures. The largest positive energy differences (least stable complexes) were observed for optimized structures in which there was evident distortion of the **FMe520** xanthene subunit either by bending or twisting; these involved conformers A and C, although destabilized complexes were found for all conformers. Negative energy differences (more stable complexes) were observed for some trials with each of the conformers (Table S4

and Fig. S17, ESI†). There do not seem to be specific interactions with cage components, but in all stabilized complexes partial projection of the **FMe520** xanthene subunit methoxy group into the larger ZIF-8 channel is seen. Frequency calculations of the optimized structures were not feasible due to the freezing of the cage subunit atomic positions. Although the trials were not exhaustive in scope, they support the experimental evidence in suggesting that **FMe520** conformations can fit inside the cage cavity in some orientations without significant destabilization.

Intracellular fluorescence imaging and cytotoxicity assays

We next investigated the ability of cells (RAW 264.7 macrophages) to become labelled with the **FMe520**@ZIF-8 composite by employing spinning disk microscopy. Indeed, metal–organic frameworks possess good biocompatibility and are able to enter cells and transport intracellularly even relatively large organic molecules, therapeutics or inorganic nanoparticles. Although the exact mechanism responsible for intracellular accumulation is not known, similarly-sized assemblies (curcumin encapsulated zeolitic imidazolate frameworks, CCM@ZIF-8) have been shown to undergo clathrin-mediated endocytosis and traffic along the endo-lysosomal pathway.[90] In our experiments, RAW cells were imaged after incubation with Alexa Fluor™ 647-conjugated dextran (dextran AF647) and a PBS dispersion of either ZIF-8 or **FMe520**@ZIF-8. Co-endocytosis with dextran AF647 was used as a control for internalization. Cells were visualized using a green channel (λ_{Ex} = 488 nm) and a far-red channel (λ_{Ex} = 637 nm); the green channel is suitable to detect the emission range of **FMe520**. These images reveal some autofluorescence in the absence of **FMe520**@ZIF-8 in cells treated with either dextran AF637 alone (A in Fig. 6) or empty ZIF-8 alongside the dextran AF637 (B in Fig. 6). Nevertheless, the mean fluorescence intensity in the green channel of cells incubated with **FMe520**@ZIF-8 is distinctively higher than cells treated with dextran AF637 alone (vehicle) or empty ZIF-8 alongside dextran AF637 (C and D in Fig. 6). This is in agreement with the successful encapsulation of the MOF-containing fluorescein. The punctuate intracellular distribution of the **FMe520**@ZIF-8 suggests their accumulation is restricted to the endo-lysosomal compartment in cells, though not as widely distributed as the dextran probe.

The cytotoxicity of the ZIF-8 containing **FMe520** was assessed with the Trypan Blue assay. This particular organic dye stains exclusively dead or dying cells and offers the opportunity to determine the fraction of living cells (viability). Specifically, the viability was determined for RAW cells either incubated with PBS or a PBS dispersion of **FMe520**@ZIF-8 (E in Fig. 6). In both instances, the cell viability remains essentially unchanged. Thus, the supramolecular construct does not have any significant toxicity on the RAW cells.

Conclusions

We have demonstrated how supramolecular strategies can be invoked to prepare a microporous fluorescent solid material
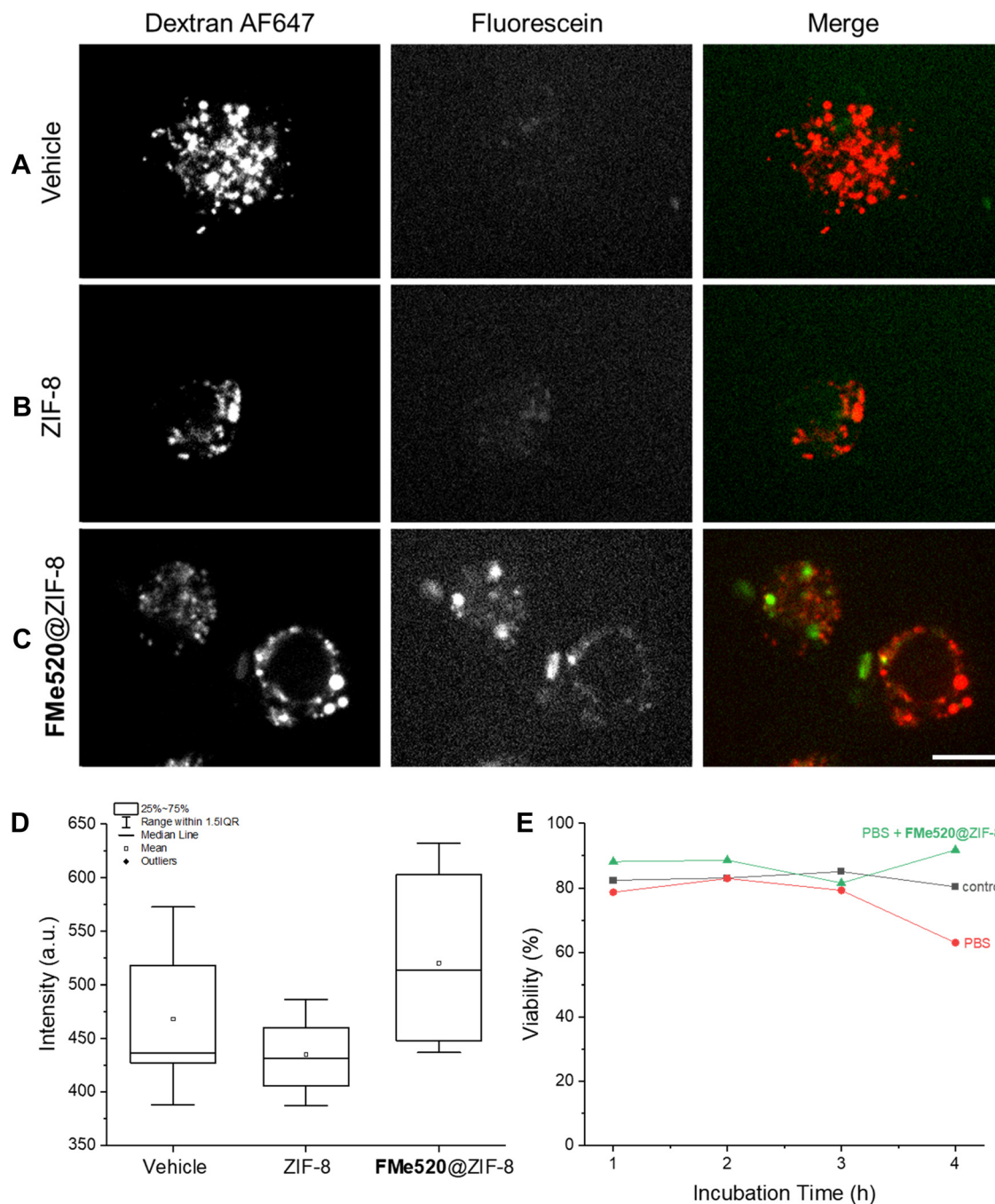
Fig. 6 Spinning disk fluorescence images (green channel, λ_{Ex} = 488 nm; far-red channel, λ_{Ex} = 637 nm, scale bar = 10 μm) of RAW 264.7 macrophages incubated with (A) dextran Alexa Fluor™ 647 alone, (B) dextran Alexa Fluor™ 647 and ZIF-8, and (C) dextran Alexa Fluor™ 647 and **FMe520**@ZIF-8. The box chart (D) represents the intensity measured in ROIs corresponding to individual cells after background subtraction. (E) Viability of RAW cells left untreated or incubated with PBS or a stock PBS dispersion of **FMe520**@ZIF-8 (15 mg mL^{-1}) for 1, 2, 3, and 4 h of incubation.

based on the fluorescein dye. The zeolitic imidazolate metal–organic framework ZIF-8 can capture a fluorescein derivative and transfer it within the interior pore structure. A reduction in the average size distribution of the MOF particles from 270 to 80 nm is observed when crystallization is conducted in the presence of the guest dye. Within the resulting constructs, the spectroscopic signatures and photophysical properties of the organic chromophore are preserved, while its photostability

and average luminescence lifetime are enhanced compared to the free dye. Moreover, encapsulation within the MOF suppresses aggregation-caused quenching phenomena that typically manifest in the solid-state. SCC-DFTB optimizations of **FMe520** conformers within a frozen ZIF-8 SOD cage subunit are consistent with **FMe520** being small enough in size to fit within the cage subunit without significant steric destabilization. Furthermore, the MOF container can be internalized by cells through endocytosis,

trapping these into endosomes and lysosomes, and permitting the intracellular detection of fluorescence. In addition, neither the framework nor the fluorophore@ZIF-8 assembly appears cytotoxic. Overall, this simple supramolecular approach to synthesizing new fluorescent constructs from separate fluorophores and commercially available reagents can evolve into a valuable protocol for the intracellular delivery and operation of functional molecular components, as well as the fabrication of solid-state fluorescent materials with improved photophysical properties. This protocol can, in principle, be adapted to other organic dyes and/or frameworks of suitable molecular dimensions, and facilitate the fabrication of new highly emissive solids. The next steps will also include the study of the fluorophore's role in the deliberate production of nanosized MOFs.

Experimental procedures

Materials and methods

All reagents were purchased from Sigma Aldrich and Fisher Scientific. Solvents were purchased from ACP. Ultrapure deionized water (MilliΩ, 18.2 MΩ) was obtained from a Millipore Purification System. Reactions were monitored by thin-layer chromatography using aluminum-backed sheets coated with 200 µm silica (60, F_{254}). SiliaFlash® P60, 40–63 mm (230–400 mesh) silica gel from SiliCycle was used for purification by column chromatography. NMR spectra were recorded at room temperature with a Bruker Avance 400 spectrometer. Steady-state absorption spectra were recorded with an Agilent Cary 60 UV-visible spectrometer, using quartz cells with a path length of 1 cm or an Agilent solid sample holder accessory. Steady-state emission spectra were recorded with an Agilent Cary Eclipse spectrometer using quartz cells or an Agilent solid sample holder accessory. Diffuse reflectance spectroscopy was performed using an Agilent Cary 5000 UV-visible spectrophotometer equipped with an internal diffuse reflectance accessory (DRA-2500). Illumination at 455 nm was executed using a portable Luzchem LEDi illuminator. Powder X-ray diffraction (PXRD) patterns were collected using a Rigaku MiniFlex600 powder diffractometer equipped with a Cu-Kα (λ = 1.540593 Å) source and a SC-70 detector. The patterns were collected in the 2θ range of 3° to 40°. Experimental PXRD patterns of ZIF-8 powder were compared to simulated PXRD pattern of ZIF-8 (CSD code VELVOY) calculated from published crystal structures using Mercury software. Crystallographic Information File was obtained from the Cambridge Structural Database (CSD). SEM images were recorded with a Hitachi SU7000 at the Ontario Centre for the Characterization of Advanced Materials (OCCAM). FTIR Diamond ATR spectra were recorded with a Cary 630 spectrometer by Agilent technologies. Electrospray ionization mass spectrometry was conducted on an Advion Expression compact mass spectrometer (CMS). Thermogravimetric analysis (TGA) was conducted on a PerkinElmer TGA 4000 under a dynamic atmosphere of air. Samples were heated to an upper-temperature limit of 900 °C at a rate of 10 °C min^{-1} and a gas flow rate of 20 mL min^{-1}. FLIM was performed using a Zeiss AxioObserver system with a x63 oil immersion objective, 479 nm LED excitation source, a 470/40 nm bandpass excitation filter and a 525/50 nm bandpass emission filter. Gain was set to 550 V for all samples, and an aqueous fluorescein solution with a known monoexponential lifetime of 4.04 ns served as a reference standard. Multifrequency recordings were made at 10 equal steps from 20–200 MHz, with 12 phase images collected at each frequency. LI-FLIM software (Lambert Instruments) was used for image acquisition and analysis, where phase modulation lifetimes were extracted based on the average of 6 ROIs for each sample.

Synthesis of FMe520

To a cleaned and oven-dried 250 mL round bottom flask equipped with a magnetic stir bar, fluorescein (3.32 g, 10 mmol) and K$_2$CO$_3$ (4.14 g, 30 mmol) were dissolved in CH$_3$CN (60 mL). Methyl iodide (1.87 mL, 30 mmol) was then added, and the mixture refluxed for 24 h at 60 °C. The solvent was evaporated under reduced pressure. The crude was diluted with saturated NaHCO$_3$ (40 mL) and extracted with CH$_2$Cl$_2$ (5 × 40 mL). The organic phases were combined and dried over Na$_2$SO$_4$, filtered, and concentrated under reduced pressure. The product was purified by column chromatography [SiO$_2$: Hexanes/EtOAc 1 : 1(v/v) with an increasing polarity gradient to CH$_2$Cl$_2$/CH$_3$OH 9 : 1 (v/v)] to obtain 0.81 g (23%) of **FMe520**. ^{1}H NMR (400 MHz, CDCl$_3$): δ 8.32 (1H, d, J = 7.6 Hz), 7.89–7.8 (2H, m), 7.45 (1H, d, J = 7.4 Hz), 7.25 (1H, s), 7.06–7.03 (2H, m), 6.95 (1H, d, J = 9.3 Hz), 6.59 (1H, d, J = 9.6 Hz), 6.52 (1H, s), 3.99 (3H, s), 3.63 (3H, s). ^{13}C {^{1}H} NMR (100 MHz, CDCl$_3$): δ 185.8, 165.6, 160.1, 155.0, 134.1, 132.7, 131.2, 130.8, 130.3, 130.0, 129.9, 129.3, 127.8, 116.7, 114.4, 114.3, 104.0, 100.0, 55.5, 55.4, 48.3.

Synthesis of ZIF-8

ZIF-8 was synthesized by combining a solution of 2-methylimidazole (73 mg, 0.89 mmol) in CH$_3$OH (15 mL) with a solution of Zn(NO$_3$)$_2$·6H$_2$O (82 mg, 0.43 mmol) in the same solvent (15 mL). The mixture was allowed to sit at ambient temperature (25 °C) for 24 hours. The product was isolated over three rounds of centrifugation (4 × 9000 rpm, 20 °C, 30 min per round) with CH$_3$OH (25 mL per round). Typical yields range from 130 to 140 mg.

Synthesis of FMe520@ZIF-8

20.7 mg (0.058 mmol) of **FMe520** were placed in a 100 mL round bottom flask and dissolved in CH$_3$OH (35 mL). Next, 205 mg (2.5 mmol) of 2-methylimidazole were added and the solution was sonicated. In a separate vessel, 246 mg (1.3 mmol) of Zn(NO$_3$)$_2$·6H$_2$O were dissolved in CH$_3$OH (30 mL) and added to the solution containing the dye and ligand. The mixture was left undisturbed for either 24 or 48 hours to obtain **FMe520@ZIF-8**, which was purified via centrifugation (4 × 9000 rpm, 20 °C, 30 min per round, CH$_3$OH) until no trace of residual dye was detected in the supernatants using absorption and emission spectroscopy. Typical yields range from 43 to 55 mg.

Cell culture, labelling, and cytotoxicity assays

Mouse RAW 264.7 macrophage cells were obtained from ATCC (ATCC TIB-71™, American Type Culture Collection, Manassas, VA, USA) and were cultured at 37 °C and 5% CO_2 in DMEM supplemented with 10% heat-inactivated fetal bovine serum (FBS; Wisent Inc., St-Bruno, QC, Canada). For experiments, cells were plated on uncoated glass coverslips and used at 50–80% confluency. Cells were washed with PBS and replenished with fresh DMEM media. Cells were then co-administered a mixture of 15 µg mL^{-1} Alexa Fluor™ 647-conjugated dextran (Invitrogen) and 20 µg mL^{-1} of either ZIF-8 or **FMe520**@ZIF-8 and incubated at 37 °C for 30 min. The media were discarded, and cells were washed once with PBS and replenished with fresh DMEM before imaging. To test cytotoxicity, RAW cells were grown in a 12-well plate, using DMEM supplemented with 10% FBS and 1% Pen/Strep (antibiotics) as growth media, to achieve 75% confluency on the day of the experiment. Cells were then washed once with 1 mL of PBS before being replenished with 1 mL of fresh growth media. Cells were left untreated or treated with PBS, or with a PBS dispersion of **FMe520**@ZIF-8 at a final concentration of 20 µg mL^{-1} and incubated for 1, 2, 3 and 4 h at 37 °C and 5% CO_2. At each time point, cells were washed with PBS, replenished with fresh media and lifted with a sterile scrapper. Cells were then mixed with Trypan Blue in a 1 : 1 ratio (5 µL cells + 5 µL dye) and left for 2 min at room temperature. This mixture was then placed on a glass slide and counted with Thermo Scientific Invitrogen Countess II AMQAX1000 Cell Counter (3–4 readings were taken for each sample).

Microscopy and image analysis

Live-cell fluorescence imaging of RAW cells was performed using a Quorum Diskovery spinning disc confocal microscope system (Quorum Technologies, Inc.) consisting of an inverted fluorescence microscope (DMi8; Leica) and equipped with a x63 oil immersion objective (1.4 NA), an Andor iXON 897 EM-CCD camera (Oxford Instruments, Belfast, UK), and illuminated through a 100 µm pinhole disc. Coverslips with cells were imaged in a microscope-mounted chamber containing DMEM supplemented with 10% FBS and maintained at 37 °C and 5% CO_2. Single plane images were acquired with the brightfield, green (λ_{Ex} = 488 nm) and far-red (λ_{Ex} = 637 nm) channels. 16-Bit images in the green channel were acquired with an exposure of 200 ms, EM gain 50 and a laser intensity 60%. 16-Bit images in the far-red channel were acquired with an exposure of 100 ms, EM gain 50, and a laser intensity set to 50%. Images were analyzed using Fiji (Image J). For representation purposes, images in the green channel were window balanced using images from the conditions yielding the highest intensity (*i.e.*, with **FMe520**@ZIF-8) to provide comparable visualization without altering the actual pixel values. Individual cells were selected as ROI, and their mean intensity was measured, followed by background subtraction.

Computational details

The Gaussian 16 suite of programs was used for all calculations (G16 Rev C.01).[91] The **FMe520** compound was investigated by geometric optimization with tight convergence criteria at the SCC-DFTB and B3LYP/6-311 + G(d,p) levels of theory[92] to determine conformer stabilities, with energy minima verified by frequency calculation. The ZIF-8 framework cage geometry was derived from the unit cell of the 100 K X-ray crystallographic structure (864309.cif),[93] omitting waters of crystallization. Calculations of the ZIF-8 cage subunit and encapsulated **FMe520** used the self-consistent charge density-functional tight-binding (SCC-DFTB) method[94] and the znorg-0-1 parameter set Slater–Koster files.[95] Geometry optimizations used tight convergence criteria.

Conflicts of interest

The authors declare no competing financial interests.

Acknowledgements

References

1 J. Della Rocca, D. Liu and W. Lin, *Acc. Chem. Res.*, 2011, **44**, 957–968.
2 H.-S. Wang, *Coord. Chem. Rev.*, 2017, **349**, 139–155.
3 D. F. Sava Gallis, L. E. S. Rohwer, M. A. Rodriguez, M. C. Barnhart-Dailey, K. S. Butler, T. S. Luk, J. A. Timlin and K. W. Chapman, *ACS Appl. Mater. Interfaces*, 2017, **9**, 22268–22277.
4 H.-S. Wang, Y.-H. Wang and Y. Ding, *Nanoscale Adv.*, 2020, **2**, 3788–3797.
5 U. Ryu, J. Yoo, W. Kwon and K. M. Choi, *Inorg. Chem.*, 2017, **56**, 12859–12865.
6 K. S. Butler, C. J. Pearce, E. A. Nail, G. A. Vincent and D. F. Sava Gallis, *ACS Appl. Mater. Interfaces*, 2020, **12**, 31217–31224.

7 D. Liu, K. Lu, C. Poon and W. Lin, *Inorg. Chem.*, 2014, **53**, 1916–1924.

8 H.-C. Zhou, J. R. Long and O. M. Yaghi, *Chem. Rev.*, 2012, **112**, 673–674.

9 J.-R. Li, J. Sculley and H.-C. Zhou, *Chem. Rev.*, 2012, **112**, 869–932.

10 S. Kitagawa, R. Kitaura and S. Noro, *Angew. Chem., Int. Ed.*, 2004, **43**, 2334–2375.

11 H. Furukawa, K. E. Cordova, M. O'Keeffe and O. M. Yaghi, *Science*, 2013, **341**, 1230444.

12 W. P. Lustig, S. Mukherjee, N. D. Rudd, A. V. Desai, J. Li and S. K. Ghosh, *Chem. Soc. Rev.*, 2017, **46**, 3242–3285.

13 M. Lv, W. Zhou, H. Tavakoli, C. Bautista, J. Xia, Z. Wang and X. Li, *Biosens. Bioelectron.*, 2021, **176**, 112947.

14 G. A. Udourioh, M. M. Solomon and E. I. Epelle, *Cell. Mol. Bioeng.*, 2021, **14**, 535–553.

15 Y. Zhao, H. Zeng, X.-W. Zhu, W. Lu and D. Li, *Chem. Soc. Rev.*, 2021, **50**, 4484–4513.

16 J. Zhou, Y. Li, W. Wang, X. Tan, Z. Lu and H. Han, *Biosens. Bioelectron.*, 2020, **164**, 112332.

17 J. Zhou, G. Tian, L. Zeng, X. Song and X. Bian, *Adv. Healthcare Mater.*, 2018, **7**, 1800022.

18 N. Bhardwaj, S. K. Bhardwaj, D. Bhatt, S. K. Tuteja, K.-H. Kim and A. Deep, *Anal. Methods*, 2019, **11**, 917–923.

19 B. A. Lakshmi and S. Kim, *Mater. Sci. Eng., C*, 2019, **105**, 110091.

20 W. Shang, L. Peng, P. Guo, H. Hui, X. Yang and J. Tian, *ACS Biomater. Sci. Eng.*, 2020, **6**, 1008–1016.

21 W. Sun, S. Li, G. Tang, Y. Luo, S. Ma, S. Sun, J. Ren, Y. Gong and C. Xie, *Int. J. Nanomed.*, 2019, **14**, 10195–10207.

22 P. Yang, Z. Chen, S. Liu, C. Qiao, Y. Xia and Z. Wang, *Biomed. Mater.*, 2021, **16**, 042011.

23 J. Yang and Y.-W. Yang, *View*, 2020, **1**, e20.

24 C. Tamames-Tabar, D. Cunha, E. Imbuluzqueta, F. Ragon, C. Serre, M. J. Blanco-Prieto and P. Horcajada, *J. Mater. Chem. B*, 2014, **2**, 262–271.

25 S. Li, L. Tan and X. Meng, *Adv. Funct. Mater.*, 2020, **30**, 1908924.

26 P. Horcajada, R. Gref, T. Baati, P. K. Allan, G. Maurin, P. Couvreur, G. Férey, R. E. Morris and C. Serre, *Chem. Rev.*, 2012, **112**, 1232–1268.

27 M. Giménez-Marqués, T. Hidalgo, C. Serre and P. Horcajada, *Coord. Chem. Rev.*, 2016, **307**, 342–360.

28 R. F. Mendes, F. Figueira, J. P. Leite, L. Gales and F. A. Almeida Paz, *Chem. Soc. Rev.*, 2020, **49**, 9121–9153.

29 S. Mandal, S. Natarajan, P. Mani and A. Pankajakshan, *Adv. Funct. Mater.*, 2021, **31**, 2006291.

30 K. K. Tanabe and S. M. Cohen, *Chem. Soc. Rev.*, 2011, **40**, 498–519.

31 Z. Wang and S. M. Cohen, *Chem. Soc. Rev.*, 2009, **38**, 1315–1329.

32 Z. Yin, S. Wan, J. Yang, M. Kurmoo and M.-H. Zeng, *Coord. Chem. Rev.*, 2019, **378**, 500–512.

33 C. He, D. Liu and W. Lin, *Chem. Rev.*, 2015, **115**, 11079–11108.

34 C. Orellana-Tavra, S. A. Mercado and D. Fairen-Jimenez, *Adv. Healthcare Mater.*, 2016, **5**, 2261–2270.

35 Y. Cui, Y. Yue, G. Qian and B. Chen, *Chem. Rev.*, 2012, **112**, 1126–1162.

36 Z. Hu, B. J. Deibert and J. Li, *Chem. Soc. Rev.*, 2014, **43**, 5815–5840.

37 Y. Cui, B. Chen and G. Qian, *Coord. Chem. Rev.*, 2014, **273–274**, 76–86.

38 D. T. de Lill, A. de Bettencourt-Dias and C. L. Cahill, *Inorg. Chem.*, 2007, **46**, 3960–3965.

39 W. P. Lustig and J. Li, *Coord. Chem. Rev.*, 2018, **373**, 116–147.

40 J. Heine and K. Müller-Buschbaum, *Chem. Soc. Rev.*, 2013, **42**, 9232–9242.

41 T. N. Nguyen, F. M. Ebrahim and K. C. Stylianou, *Coord. Chem. Rev.*, 2018, **377**, 259–306.

42 M. D. Allendorf, C. A. Bauer, R. K. Bhakta and R. J. T. Houk, *Chem. Soc. Rev.*, 2009, **38**, 1330–1352.

43 H. Kaur, S. Sundriyal, V. Pachauri, S. Ingebrandt, K.-H. Kim, A. L. Sharma and A. Deep, *Coord. Chem. Rev.*, 2019, **401**, 213077.

44 Y. Cui, F. Zhu, B. Chen and G. Qian, *Chem. Commun.*, 2015, **51**, 7420–7431.

45 É. Whelan, F. W. Steuber, T. Gunnlaugsson and W. Schmitt, *Coord. Chem. Rev.*, 2021, **437**, 213757.

46 Y. Liu, X.-Y. Xie, C. Cheng, Z.-S. Shao and H.-S. Wang, *J. Mater. Chem. C*, 2019, **7**, 10743–10763.

47 D. Zou, J. Zhang, Y. Cui and G. Qian, *Dalton Trans.*, 2019, **48**, 6669–6675.

48 V. Glembockyte, M. Frenette, C. Mottillo, A. M. Durantini, J. Gostick, V. Štrukil, T. Friščić and G. Cosa, *J. Am. Chem. Soc.*, 2018, **140**, 16882–16887.

49 K. Hirai, T. Kitagawa, H. Fujiwara, J. Pirillo, Y. Hijikata, T. Inose and H. Uji-i, *Chem. Commun.*, 2020, **56**, 9651–9654.

50 Z. Wei, D. Chen, Z. Guo, P. Jia and H. Xing, *Inorg. Chem.*, 2020, **59**, 5386–5393.

51 N. Zhang, D. Zhang, J. Zhao and Z. Xia, *Dalton Trans.*, 2019, **48**, 6794–6799.

52 Y. Cui, R. Song, J. Yu, M. Liu, Z. Wang, C. Wu, Y. Yang, Z. Wang, B. Chen and G. Qian, *Adv. Mater.*, 2015, **27**, 1420–1425.

53 H. Cai, W. Lu, C. Yang, M. Zhang, M. Li, C.-M. Che and D. Li, *Adv. Opt. Mater.*, 2019, **7**, 1801149.

54 A. K. Chaudhari and J.-C. Tan, *Adv. Opt. Mater.*, 2020, **8**, 1901912.

55 H. Li, W. Yang and Q. Pan, *RSC Adv.*, 2020, **10**, 33879–33893.

56 K. Sumida, D. L. Rogow, J. A. Mason, T. M. McDonald, E. D. Bloch, Z. R. Herm, T.-H. Bae and J. R. Long, *Chem. Rev.*, 2012, **112**, 724–781.

57 A. Dhakshinamoorthy, M. Alvaro and H. Garcia, *Chem. Commun.*, 2012, **48**, 11275–11288.

58 J. M. Simmons, H. Wu, W. Zhou and T. Yildirim, *Energy Environ. Sci.*, 2011, **4**, 2177–2185.

59 R. Banerjee, A. Phan, B. Wang, C. Knobler, H. Furukawa, M. O'Keeffe and O. M. Yaghi, *Science*, 2008, **319**, 939–943.

60 M. S. Denny, J. C. Moreton, L. Benz and S. M. Cohen, *Nat. Rev. Mater.*, 2016, **1**, 16078.

61 H. Sakamoto, A. Ito and M. Ohtani, *Mater. Adv.*, 2022, **3**, 2011–2017.

62 J.-P. Zhang, Y.-B. Zhang, J.-B. Lin and X.-M. Chen, *Chem. Rev.*, 2012, **112**, 1001–1033.

63 K. S. Park, Z. Ni, A. P. Côté, J. Y. Choi, R. Huang, F. J. Uribe-Romo, H. K. Chae, M. O'Keeffe and O. M. Yaghi, *Proc. Natl. Acad. Sci. U. S. A.*, 2006, **103**, 10186–10191.

64 M. Hoop, C. F. Walde, R. Riccò, F. Mushtaq, A. Terzopoulou, X.-Z. Chen, A. J. DeMello, C. J. Doonan, P. Falcaro, B. J. Nelson, J. Puigmartí-Luis and S. Pané, *Appl. Mater. Today*, 2018, **11**, 13–21.

65 *The Molecular Probes Handbook—A Guide to Fluorescent Probes and Labeling Technologies*, ed. I. D. Johnson, Life Technologies Corporation, 11th edn, 2010.

66 K. Kuwayama, S. Miyauchi, R. Tateoka, H. Abe and N. Kamo, *Biochem. Pharmacol.*, 2002, **63**, 81–88.

67 K. Berginc, S. Žakelj, L. Levstik, D. Uršič and A. Kristl, *Eur. J. Pharm. Biopharm.*, 2007, **66**, 281–285.

68 Y. Zhou, J. Y. Li, K. H. Chu, K. Liu and C. Yao, *Chem. Commun.*, 2012, **48**, 4677–4679.

69 D. Yan, Y. Tang, H. Lin and D. Wang, *Sci. Rep.*, 2015, **4**, 4337.

70 Y. Wen, T. Sheng, X. Zhu, C. Zhuo, S. Su, H. Li, S. Hu, Q.-L. Zhu and X. Wu, *Adv. Mater.*, 2017, **29**, 1700778.

71 T.-T. Han, J. Yang, Y.-Y. Liu and J.-F. Ma, *Microporous Mesoporous Mater.*, 2016, **228**, 275–288.

72 J. V. Morabito, L.-Y. Chou, Z. Li, C. M. Manna, C. A. Petroff, R. J. Kyada, J. M. Palomba, J. A. Byers and C.-K. Tsung, *J. Am. Chem. Soc.*, 2014, **136**, 12540–12543.

73 Z. Li, T. M. Rayder, L. Luo, J. A. Byers and C.-K. Tsung, *J. Am. Chem. Soc.*, 2018, **140**, 8082–8085.

74 T. Wang, S. Li, Z. Zou, L. Hai, X. Yang, X. Jia, A. Zhang, D. He, X. He and K. Wang, *J. Mater. Chem. B*, 2018, **6**, 3914–3921.

75 H. Zheng, Y. Zhang, L. Liu, W. Wan, P. Guo, A. M. Nyström and X. Zou, *J. Am. Chem. Soc.*, 2016, **138**, 962–968.

76 K. A. S. Usman, J. W. Maina, S. Seyedin, M. T. Conato, L. M. Payawan, L. F. Dumée and J. M. Razal, *NPG Asia Mater.*, 2020, **12**, 58.

77 C. Eggeling, J. Widengren, R. Rigler and C. A. M. Seidel, in *Applied Fluorescence in Chemistry, Biology and Medicine*, Springer, Berlin, Heidelberg, 1999, pp. 193–240.

78 C. Chizallet and N. Bats, *J. Phys. Chem. Lett.*, 2010, **1**, 349–353.

79 S. B. Zadvarzi, M. Khavarpour, S. M. Vahdat, S. M. Baghbanian and A. S. Rad, *Int. J. Biol. Macromol.*, 2021, **168**, 428–441.

80 B. Ba Mohammed, H. Lgaz, A. A. Alrashdi, K. Yamni, N. Tijani, Y. Dehmani, H. El Hamdani and I.-M. Chung, *Arabian J. Chem.*, 2021, **14**, 102897.

81 V. Anh Tran, K. B. Vu, T.-T. Thi Vo, V. Thuan Le, H. H. Do, L. G. Bach and S.-W. Lee, *Appl. Surf. Sci.*, 2021, **538**, 148065.

82 H. Amrouche, S. Aguado, J. Pérez-Pellitero, C. Chizallet, F. Siperstein, D. Farrusseng, N. Bats and C. Nieto-Draghi, *J. Phys. Chem. C*, 2011, **115**, 16425–16432.

83 C. Wu, D. Xie, Y. Mei, Z. Xiu, K. M. Poduska, D. Li, B. Xu and D. Sun, *Phys. Chem. Chem. Phys.*, 2019, **21**, 17571–17577.

84 A. Thomas, K. R. Maiyelvaganan, S. Kamalakannan and M. Prakash, *ACS Omega*, 2019, **4**, 22655–22666.

85 R. Darvishi and E. Pakizeh, *Int. J. Polym. Sci.*, 2020, **2020**, 1–12.

86 I. Ul Haq, S. Hui Li, H.-G. Zhen, R. Khan, A.-S. Zhang and Z.-P. Zhao, *Chem. Eng. J.*, 2020, **402**, 125980.

87 C. L. Hobday, C. H. Woodall, M. J. Lennox, M. Frost, K. Kamenev, T. Düren, C. A. Morrison and S. A. Moggach, *Nat. Commun.*, 2018, **9**, 1429.

88 R. J. Verploegh, A. Kulkarni, S. E. Boulfelfel, J. C. Haydak, D. Tang and D. S. Sholl, *J. Phys. Chem. C*, 2019, **123**, 9153–9167.

89 X. Dong, S. Chen, Y. Chen and M. Zhang, *Comput. Theor. Chem.*, 2019, **1158**, 41–46.

90 A. Tiwari, A. Singh, N. Garg and J. K. Randhawa, *Sci. Rep.*, 2017, **7**, 12598.

91 M. J. Frisch, G. W. Trucks, H. B. Schlegel, G. E. Scuseria, M. A. Robb, J. R. Cheeseman, G. Scalmani, V. Barone, G. A. Petersson and H. Nakatsuji, *et al.*, *Gaussian 16, Rev. C. 01*, 2016.

92 P. J. Stephens, F. J. Devlin, C. F. Chabalowski and M. J. Frisch, *J. Phys. Chem.*, 1994, **98**, 11623–11627.

93 W. Morris, C. J. Stevens, R. E. Taylor, C. Dybowski, O. M. Yaghi and M. A. Garcia-Garibay, *J. Phys. Chem. C*, 2012, **116**, 13307–13312.

94 M. Elstner, D. Porezag, G. Jungnickel, J. Elsner, M. Haugk, T. Frauenheim, S. Suhai and G. Seifert, *Phys. Rev. B: Condens. Matter Mater. Phys.*, 1998, **58**, 7260–7268.

95 N. H. Moreira, G. Dolgonos, B. Aradi, A. L. da Rosa and T. Frauenheim, *J. Chem. Theory Comput.*, 2009, **5**, 605–614.